Dimensionality-Induced Change in Topological Order in Multiferroic Oxide Superlattices

Megan E. Holtz [1,2] Elliot S. Padgett [1] Rachel Steinhardt [2] Charles M. Brooks,[2] Dennis Meier [3]
Darrell G. Schlom [2,4,5] David A. Muller [1,4] and Julia A. Mundy[1,6,*]

[1]*School of Applied and Engineering Physics, Cornell University, Ithaca, New York 14853, USA*
[2]*Department of Materials Science and Engineering, Cornell University, Ithaca, New York 14853, USA*
[3]*Department of Materials Science and Engineering, Norwegian University of Science and Technology, NTNU,
7491 Trondheim, Norway*
[4]*Kavli Institute at Cornell for Nanoscale Science, Ithaca, New York 14853, USA*
[5]*Leibniz-Institut für Kristallzüchtung, Max-Born-Straße 2, 12489 Berlin, Germany*
[6]*Department of Physics, Harvard University, Cambridge, Massachusetts 02138, USA*

We construct ferroelectric $(\text{LuFeO}_3)_m/(\text{LuFe}_2\text{O}_4)$ superlattices with varying index m to study the effect of confinement on topological defects. We observe a thickness-dependent transition from neutral to charged domain walls and the emergence of fractional vortices. In thin LuFeO_3 layers, the volume fraction of domain walls grows, lowering the symmetry from $P6_3cm$ to $P3c1$ before reaching the nonpolar $P6_3/mmc$ state, analogous to the group-subgroup sequence observed at the high-temperature ferroelectric to paraelectric transition. Our study shows how dimensional confinement stabilizes textures beyond those in bulk ferroelectric systems.

Understanding transitions between a disordered and ordered phase was a major triumph of 20th century physics. In nonadiabatic transitions, the Kibble-Zurek framework describes a transition in which spontaneous symmetry breaking in disconnected regions creates topological defects [1,2]. While this model was developed in cosmology, it found application to a variety of solid-state systems, playing a central role in understanding phase transitions ranging from superfluid ^{4}He to high-temperature superconductors. In particular, ferroelectric materials have topological defects such as vortices and domain walls, which have been used to study otherwise inaccessible topological phenomena in the same universality class, answering cosmology-related questions [3–5]. The topological defects can be imaged at the micron scale with scanning probe or optical microscopy [6–9] or at the atomic scale with transmission electron microscopy [10–13]. In addition to their significance for fundamental research, these vortices and domain walls exhibit emergent functional properties due to their unique electrostatics, representing nanoscale objects with distinct insulating, conducting, or magnetic properties that are not present in the homogeneous bulk phases [7,8,12,14–16].

Topologically rich structures in perovskite ferroelectric systems have recently been created and manipulated using geometric confinement to tune the interplay between strain and depolarization fields. Nanostructured systems such as ferroelectric disks, rods, and composites have displayed vortices, skyrmions, and waves [17–20]. Precise epitaxial growth can further generate new metastable phases hidden in the energy landscape and has been recently used to form ferroelectric-paraelectric superlattices that generate ferroelectric vortices [21] and polar skyrmions [22]. This opened the door to studying the chirality, negative capacitance, and piezo-electric responses in these topological structures [23–25]. These studies focused on "soft" ferroelectrics, where the spontaneous polarization rotates from the direction it has in the bulk structure in response to geometric confinement.

Here, we present atomically precise $(\text{LuFeO}_3)_m/(\text{LuFe}_2\text{O}_4)$ superlattices synthesized by reactive-oxide molecular beam epitaxy [26] as a unique synthetic construction to manipulate the existing topological textures in uniaxial ferroelectrics. Hexagonal LuFeO_3 is an improper ferroelectric that is isostructural to a class of materials including hexagonal manganites, gallates, indates, and tungsten bronzes. It has a robust ferroelectric polarization for temperatures up to 1020 K [27–30] and is a canted antiferromagnet below 147 K [31]. We layer LuFeO_3 with LuFe_2O_4, which is epitaxially matched to LuFeO_3 but is nonpolar in the bulk [32,33], and has a ferrimagnetic moment below 240 K [34], which in these $(\text{LuFeO}_3)_m/(\text{LuFe}_2\text{O}_4)$ superlattices creates a room-temperature multiferroic phase as previously reported [26,35]. In this work, we focus on the effect of confinement of the improper ferroelectric order using high-angle annular dark field (HAADF) scanning transmission electron microscopy (STEM) to measure the polar displacements and the improper order parameter [26,36] and map the domain walls and the underlying energy landscape. These
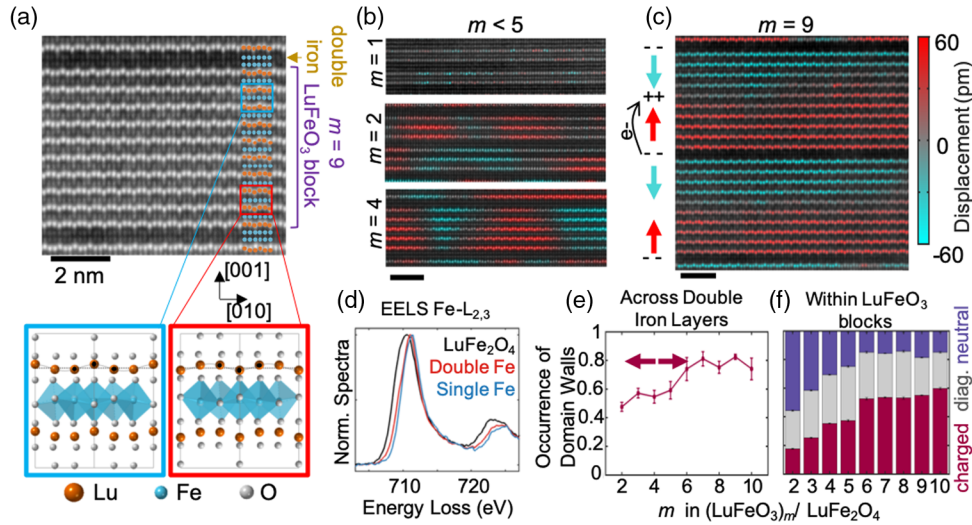
FIG. 1. (a) HAADF STEM image of an $m = 9$ $(LuFeO_3)_m/(LuFe_2O_4)$ superlattice, where bright (dark) contrast indicates lutetium (iron) atomic columns. The lower panels show a cartoon of the crystal structure. A sinusoidal curve fits the lutetium displacements, giving the amplitude Q. The phase Φ, reflecting the in-plane apical oxygen rotations, can also be retrieved from the phase of the atomic displacements, as previously done in Ref. [12]. (b),(c) Polarization color overlay, with cyan indicating polarization down and red indicating polarization up, for (b) $m = 1, 2$, and 4, and (c) $m = 9$, where head-to-head walls fall in the middle of the LuFeO$_3$ block. (d) EELS spectra of the Fe-$L_{2,3}$ edge of the double iron layers and single iron layers (the LuFeO$_3$ block) in an $m = 7$ superlattice compared to that of LuFe$_2$O$_4$. (e) The fractional occurrence of the tail-to-tail configuration across the double iron layer, per in-plane distance along the double iron layer. (f) Fractional occurrence of neutral walls (angles $>60°$ from horizontal), charged walls (angles $<30°$), and diagonal walls ($30°60°$) within the LuFeO$_3$ block, per in-plane distance along the block.

measurements show that varying the thickness of LuFeO$_3$ changes the topological ordering and symmetries present in the system.

As shown in Fig. 1(a), the improper ferroelectric polarization in LuFeO$_3$ is driven by a tilting of the iron-oxygen trigonal bipyramids which results in a polar "up-up-down" $(+P)$ or "down-down-up" $(-P)$ displacement of the lutetium atoms [37,38]. The combination of the trimerization (breaking Z_3 symmetry) and polar distortion (breaking Z_2 symmetry) leads to a net Z_6 symmetry. The primary order parameter responsible for the symmetry breaking can be described by $Q = (Q\cos\Phi, Q\sin\Phi)$ where Q is the amplitude of the distortion, and the phase Φ describes the in-plane displacements of the apical oxygens, which takes one of six discrete values $\Phi_n = n\pi/3$, $n = 0, 1, \ldots, 5$, in the polar $P6_3cm$ phase [13,28,39–41]. A lower symmetry state exists where the phase Φ varies continuously ($P3c1$), while the higher symmetry state with no distortions ($Q = 0$) gives the nonpolar $P6_3/mmc$ state [13,41]. The polarization arises due to a coupling to Q in the Landau free energy [$\sim Q^3 P \cos(3\Phi)$] [38,39,42].

Figures 1(b) and 1(c) show the polarization as color overlays as the thickness m of the LuFeO$_3$ is increased (Supplemental Material [43], Fig. 1 shows P, Q, and Φ images). The index m corresponds to the number of formula-unit-thick LuFeO$_3$ layers in each repeat of the superlattice. Consistent with our previous report [26], we observe consistent polar distortions for $m \geq 2$ [Fig. 1(b)].

The domains shown in Fig. 1(b) for $m = 2, 4$ are small with a mixture of neutral and charged walls (larger field-of-view images are in Supplemental Material [43], Fig. 2). As the thickness of the LuFeO$_3$ layer is increased, the domain structure becomes more coherent. In the $m = 9$ sample in Fig. 1(c), there are consistent polarization down domains at the top of the LuFeO$_3$ block, and polarization up domains at the bottom (larger field-of-view images are in Supplemental Material [43], Fig. 3). This pattern at high m enforces a tail-to-tail polarization configuration ($\leftarrow \rightarrow$) across the LuFe$_2$O$_4$ layer, and a head-to-head domain wall ($\rightarrow \leftarrow$) confined within the LuFeO$_3$ block.

Charged polarization configurations are typically energetically costly and only appear in isostructural systems such as bulk hexagonal manganites because of the topologically protected sixfold vortices. No vortices are observed that would prevent the material from only forming energetically favorable neutral walls, yet the charged head-to-head walls persist at high m, indicating that sixfold vortices are not imperative to form charged domain walls in this structure. Here, we find the electrostatics of the superlattice play a critical role in stabilizing the domain walls. The double iron layers in the material nominally have an average iron valence of 2.5+, compared to 3+ in the LuFeO$_3$ block. Previously, density functional theory (DFT) results on this system have shown hole doping of the double iron layer is energetically favorable, simultaneously creating a tail-to-tail polarization configuration which becomes increasingly stabilized with larger m [26], as
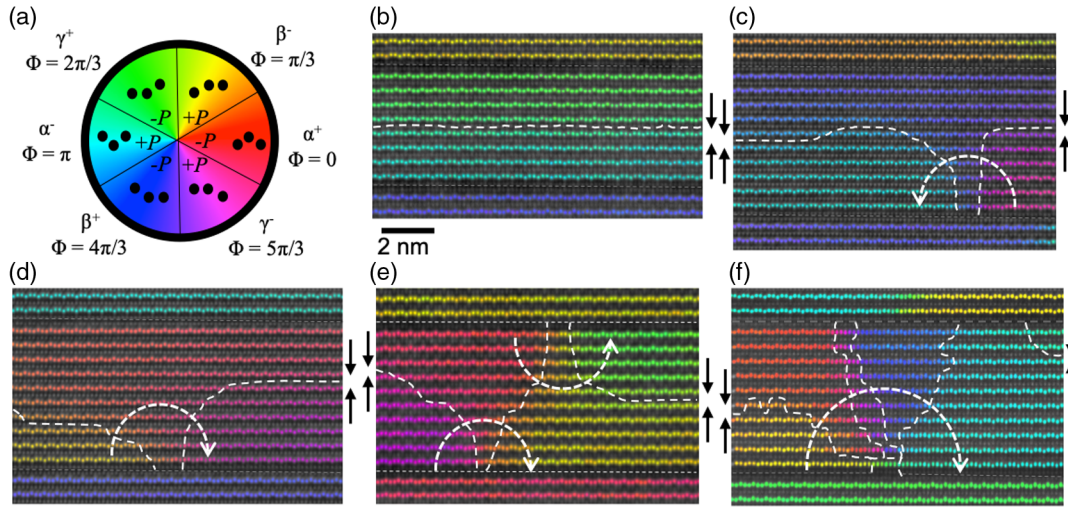
FIG. 2. Φ overlay of STEM images showing the domain structure in $(LuFeO_3)_m/(LuFe_2O_4)$ superlattices for large m ($m = 7$, 9). (a) Cartoon of the projection of lutetium positions for different Φ, with the color corresponding to the color overlays. (b) A stable charged domain wall, with black arrows showing polarization directions. (c),(d) At the end of a domain in plane, the phase rotates clockwise or anticlockwise (white arrows), forming half vortices and antivortices to maintain the charged domain wall configuration. (e) For short in-plane domains, the phase can first wrap on one neighboring double iron layer and then the other. (f) Rarely, a vortex with five domains can be observed.

illustrated schematically in Fig. 1(c). An electron energy loss spectroscopy (EELS) measurement of the iron valence [Fig. 1(d) and Supplemental Material [43], Fig. 4] shows that in the double layers of the superlattice the iron valence is reduced slightly compared to the $LuFeO_3$ block, but remains higher than the 2.5+ which is nominally observed in $LuFe_2O_4$. This indicates hole doping in the double iron layer. The DFT combined with the EELS measurements indicate that electrostatics in this confined system generate to generate the charged domain wall pattern.

We performed analysis of over $14\,000$ nm^2 ($142\,640$ atomic columns) to generate robust statistics over $m = 1$ to 10. Consistent with the qualitative observations, the tail-to-tail polarization configuration is formed across most of the double iron layers [Fig. 1(e)], with increasing regularity for increasing m. The consequence is a propensity for head-to-head walls in the $LuFeO_3$ block, with higher regularity for higher m (Supplemental Material [43], Fig. 5). Further, charged head-to-head domain walls are stabilized in the thicker layers due to their unique electrostatics [Fig. 1(f)], becoming the dominant wall type for $m > 5$. As the confinement is increased, the size of the domains shrinks [with the in-plane length of the charged domain walls decreasing linearly with decreasing m—Supplemental Material [43], Fig 5(e)], and the otherwise more energetically favorable neutral domain walls become relatively more prevalent for $m < 4$ [Fig. 1(f)].

This regular domain architecture is not observed in thin $LuFeO_3$ grown between paraelectric layers of $InFeO_3$ (Supplemental Material [43], Fig. 6) or in ultrathin epitaxial films [44], which exhibit suppression of ferroelectric order due to clamping at the interface. Additionally, $LuFeO_3$ thin films grown on YSZ are monodomain [Supplemental Material [43], Figs. 6(g) and 6(h) and [30]], as are thin films of $YMnO_3$ [44]. In our work, no vortices have been observed in $LuFeO_3$ up to thicknesses of 200 nm, indicating that our superlattices with layers thinner than 6 nm are well under the critical thickness for spontaneous vortex formation. In this work, no lattice strain or depolarizing field is present between the $LuFeO_3$ and the $LuFe_2O_4$ to suppress ferroelectric order (Supplemental Material [43], Fig. 7). The $(LuFeO_3)_m/(LuFe_2O_4)$ synthetic construct thus provides us with an experimental system that stabilizes and confines charged domain walls, which is distinct from simply considering ultrathin ferroelectric layers.

Analysis of the STEM images allows us to measure the primary order parameter (Q, Φ) that drives the polarization configuration in the $(LuFeO_3)_m/(LuFe_2O_4)$ superlattices [12]. Figure 2(a) shows the six trimerization domains corresponding to the Z_6 symmetry. The HAADF STEM images are overlaid with the color scheme in Figs. 2 and 3, for larger and smaller m, respectively. Similar to bulk hexagonal manganites, we observe a phase change $\Delta\Phi = \pm\pi/3$ at domain walls within the $LuFeO_3$ blocks, for all walls within error in $m > 3$ and for $>90\%$ of walls for $m = 2$, 3 [Supplemental Material [43], Fig. 5(d)]—the exceptions to this may be stabilized by the presence of defects in the weakly polar energy landscape. We do not observe a correlation of the phase across the $LuFe_2O_4$ beyond enforcing a tail-to-tail polarization configuration [Supplemental Material [43], Fig. 5 (c)], so each $LuFeO_3$ block can be considered as an isolated, quasi-two-dimensional system of determined thickness.

In our images of superlattices with $m > 4$, such as shown in Fig. 2, we observe "half-vortices" composed of three out

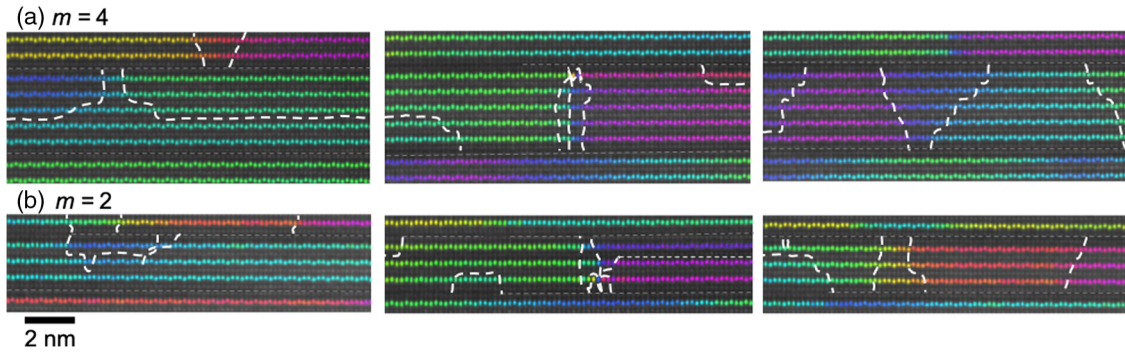FIG. 3. The order parameter Φ as a color overlay on the HAADF STEM images for small m ($m = 4, 2$) where the neutral domain walls are observed with more equal occurrence. (a) for $m = 4$, we see a fairly equal coexistence of charged ferroelectric domain walls (left), and neutral + diagonal domain walls forming stripe patterns (right). We also see irregular numbers of domains coming together to a point in the middle image. (b) In the $m = 2$ case, we see smaller areas of charged domain walls (left) and more neutral walls forming in a stripe pattern (right). We also observe unusual numbers of domains intersecting (middle).

of the six possible domain states sketched in Fig. 2(a). The "core" of such fractional vortices is pinned to the double iron layers as displayed in Figs. 2(c) and 2(d). In Fig. 2(e), two half-vortices appear side by side, with phases wrapping in the same direction. The systematic formation of such half-vortices in $(LuFeO_3)_m/(LuFe_2O_4)$ allows the system to stabilize head-to-head walls within the $LuFeO_3$ blocks, while keeping a tail-to-tail configuration across the $LuFe_2O_4$ layers. This behavior is fundamentally different from analogous bulk systems where the structural trimerization enforces sixfold vortices. While the splitting of structural vortices into "fragmented vortices" has been predicted to occur in systems away from the ground state [40], the observed correlation between preferred domain wall orientations and half-vortices is unexpected. Rarely, five domains come together at a point, shown in Fig. 2(f), possibly stabilized by defects. The electrostatics which drive the tail-to-tail polarization configuration across the $LuFe_2O_4$ layer discourage or prohibit the formation of a full vortex—indeed, as noted above no bulklike full vortices have been observed in this thin-film system for $LuFeO_3$ thicknesses up to 200 nm. Interestingly, as the phases wrap around the fractional vortices, they progress from Z_6 symmetry toward a U(1) symmetry near the core (Supplemental Material [43], Fig. 8), analogous to the sixfold vortices in hexagonal manganites [12].

In the bulk case, the primary order parameter related to the structural symmetry breaking drives the formation of vortices, which enforce electrostatically unfavorable charged ferroelectric domain walls. In this system, the charged domain walls appear to codetermine the topological feature formation, favoring fractional vortices. The appearance of these "fractional" vortices suggests that the impact of electrostatics in the $(LuFeO_3)_m/(LuFe_2O_4)$ superlattices is a stronger influence than in the isostructural bulk system, softening the rigid hierarchy of energy scales.

In thinner layers, as the confinement of the $LuFeO_3$ layer is increased, small domains with neutral domain walls are increasingly prevalent. Images of the $m = 2$ and 4 structures are shown in Fig. 3. For $m = 4$ in Fig. 3(a), there are charged domain walls and fractional vortices, but also stripe patterns where the phase progresses across the in-plane direction of the sample, similar to states observed under strain in bulk crystals [45] but in this case, without strain. Tail-to-tail polarization orientation is not always enforced across the double iron layer. For $m = 2$ in Fig. 3(b), we observe more instances of the topological stripe formation (with gradual phase winding, Supplemental Material [43], Fig. 9), although charged domain walls can also be found.

There is a resulting change to the global symmetry as the topological defects occupy an increasing fraction of the $LuFeO_3$ material with decreasing m. Figure 4(a) displays histograms of the logarithm of the occurrences of the structural order parameter, which maps the free energy landscape [12]. For $m \geq 4$, the domains have a well-defined energy landscape with six minima and Z_6 ($P6_3cm$) symmetry as expected. Here, intermediate states between the six wells corresponding to the domain walls. For $m = 1$, we observe the paraelectric state, corresponding to $P6_3/mmc$ symmetry. Interestingly, for $m = 2$, we observe a fairly uniform distribution of the structural order parameter, which we might expect for a state with $P3c1$ symmetry, with values at low Q indicating some contribution from paraelectric states. Likewise, the $m = 3$ state shows slightly more weight in the ferroelectric wells, while also showing some contribution from paraelectric states. These distributions are integrated from many images and reflect the nonuniformity of the sample.

As domain walls overlap within 2–3 nm of a vortex core in hexagonal $ErMnO_3$, U(1) symmetry emerges [12]. In these superlattices, the confinement length for $m = 2$ and 3 is similar to the domain wall width (Supplemental Material [43], Fig. 10), and the domain walls similarly overlap. For the $m = 2$ case, we observe local, atomic-scale polar distortions, but due to the abundance of domain walls, an
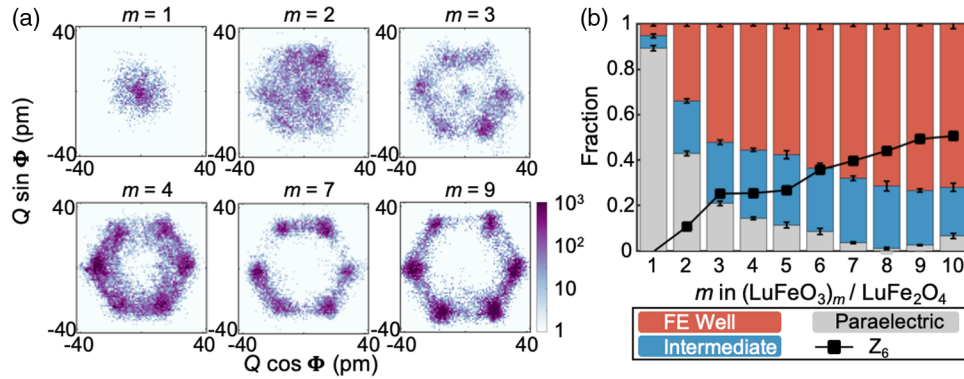
FIG. 4. (a) Histograms of the order parameter for different m in $(LuFeO_3)_m/(LuFe_2O_4)$ superlattices, with the logarithm of the occurrences plotted. $m = 1$ shows a parabolic well, consistent with a paraelectric order parameter distribution. For $m = 2$ and 3, Q is slightly larger and the values of Φ are widely spread, indicating a combination of ferroelectric domain and intermediate Φ states. For $m = 4$, the six ferroelectric domains are visible while maintaining a large fraction of intermediate states. For $m = 7$ and 9, the six ferroelectric domains comprise the majority of the observed states, and the Q value is higher. (b) Relative amount of states in ferroelectric (FE) wells vs in the intermediate states (between wells) vs the paraelectric state. The difference between the states in the well and in the intermediate states tracks the relative amount of Z_6 symmetry.

overall $P3c1$ symmetry. This group-subgroup sequence is reminiscent of bulk ferroelectric transitions observed in $YMnO_3$, where above the ferroelectric transition temperature, the average structure has $P6_3/mmc$ symmetry, while pair distribution analysis suggests that there are local fluctuations that lower the local symmetry to $P3c1$ [41]. The important difference is that the transition in $(LuFeO_3)_m/(LuFe_2O_4)$ superlattices is driven by confinement and not by an increase in temperature as it is the case in $YMnO_3$. The transition with confinement is quantified in Fig. 4(b). We observe a crossover in the dominant occupied states: the paraelectric state is dominant for $m = 1$; the paraelectric, ferroelectric well, and in-between well "intermediate" states are roughly balanced for $m = 2$; and the ferroelectric well states are most prevalent for $m > 3$.

In conclusion, we have demonstrated atomic-scale control of domain wall placement in the $(LuFeO_3)_m/(LuFe_2O_4)$ superlattice system, which further provides insight into the topology and symmetry of uniaxial ferroelectrics under dimensional confinement. In the thicker $LuFeO_3$ blocks, the topological defects consist largely of charged domain walls with "fractional" vortices pinned on the boundary $LuFe_2O_4$ layers—suggesting that the electrostatics imposed by the superlattice drive charged domain wall formation and the resulting threefold vortices. This charged domain wall pattern is disrupted for thinner $LuFeO_3$ blocks, where smaller domains with neutral domain walls prevail. As the domain walls comprise more of the material, an emergent $P3c1$ symmetry is observed for $m = 2$ before becoming paraelectric for $m = 1$. We image this transition with atomic-scale resolution, observing both the local displacements and the average symmetry from sampling the overall energy landscape. This provides direct and simultaneous imaging of the symmetry-lowering transition in confined $LuFeO_3$ layers. Moreover, as the vortex cores in these materials

were previously associated with fractional electronic charge and quantized magnetic flux, highly confined vortex and fractional vortex states could display interesting physics and produce novel functionality.

*Corresponding author.
mundy@fas.harvard.edu

[1] T. W. B. Kibble, Topology of cosmic domains and strings, J. Phys. A. **9**, 1387 (1976).

[2] W. H. Zurek, Cosmological experiments in superfluid helium?, Nature (London) **317**, 505 (1985).

[3] S. M. Griffin, M. Lilienblum, K. T. Delaney, Y. Kumagai, M. Fiebig, and N. A. Spaldin, Scaling Behavior and Beyond

Equilibrium in the Hexagonal Manganites, Phys. Rev. X **2,** 041022 (2012).

[4] S.-Z. Lin, X. Wang, Y. Kamiya, G.-W. Chern, F. Fan, D. Fan, B. Casas, Y. Liu, V. Kiryukhin, W. H. Zurek, C. D. Batista, and S.-W. Cheong, Topological defects as relics of emergent continuous symmetry and Higgs condensation of disorder in ferroelectrics, Nat. Phys. **10,** 970 (2014).

[5] Q. N. Meier, M. Lilienblum, S. M. Griffin, K. Conder, E. Pomjakushina, Z. Yan, E. Bourret, D. Meier, F. Lichtenberg, E. K. H. Salje, N. A. Spaldin, M. Fiebig, and A. Cano, Global Formation of Topological Defects in the Multiferroic Hexagonal Manganites, Phys. Rev. X **7,** 041014 (2017).

[6] M. Fiebig, T. Lottermoser, D. Fröhlich, A. V. Goltsev, and R. V. Pisarev, Observation of coupled magnetic and electric domains, Nature (London) **419,** 818 (2002).

[7] T. Choi, Y. Horibe, H. T. Yi, Y. J. Choi, W. Wu, and S.-W. Cheong, Insulating interlocked ferroelectric and structural antiphase domain walls in multiferroic $YMnO_3$, Nat. Mater. **9,** 253 (2010).

[8] D. Meier, J. Seidel, a. Cano, K. Delaney, Y. Kumagai, M. Mostovoy, N. a. Spaldin, R. Ramesh, and M. Fiebig, Anisotropic conductance at improper ferroelectric domain walls, Nat. Mater. **11,** 284 (2012).

[9] W. Wu, Y. Horibe, N. Lee, S.-W. Cheong, and J. R. Guest, Conduction of Topologically Protected Charged Ferroelectric Domain Walls, Phys. Rev. Lett. **108,** 077203 (2012).

[10] Q. H. Zhang, L. J. Wang, X. K. Wei, R. C. Yu, L. Gu, A. Hirata, M. W. Chen, C. Q. Jin, Y. Yao, Y. G. Wang, and X. F. Duan, Direct observation of interlocked domain walls in hexagonal $RMnO_3$ ($R = $ Tm, Lu), Phys. Rev. B **85,** 2 (2012).

[11] T. Matsumoto, R. Ishikawa, T. Tohei, H. Kimura, Q. Yao, H. Zhao, X. Wang, D. Chen, Z. Cheng, N. Shibata, and Y. Ikuhara, Multivariate statistical characterization of charged and uncharged domain walls in multiferroic hexagonal $YMnO_3$ single crystal visualized by a spherical aberration-corrected STEM, Nano Lett. **13,** 4594 (2013).

[12] M. E. Holtz, K. Shapovalov, J. A. Mundy, C. S. Chang, Z. Yan, E. Bourret, D. A. Muller, D. Meier, and A. Cano, Topological defects in hexagonal manganites: inner structure and emergent electrostatics, Nano Lett. **17,** 5883 (2017).

[13] F.-T. Huang, X. Wang, S. M. Griffin, Y. Kumagai, O. Gindele, M.-W. Chu, Y. Horibe, N. A. Spaldin, and S.-W. Cheong, Duality of Topological Defects in Hexagonal Manganites, Phys. Rev. Lett. **113,** 267602 (2014).

[14] Y. Geng, N. Lee, Y. J. Choi, S. W. Cheong, and W. Wu, Collective magnetism at multiferroic vortex domain walls, Nano Lett. **12,** 6055 (2012).

[15] J. A. Mundy, J. Schaab, Y. Kumagai, A. Cano, M. Stengel, I. P. Krug, D. M. Gottlob, H. Doğanay, M. E. Holtz, R. Held, Z. Yan, E. Bourret, C. M. Schneider, D. G. Schlom, D. A. A. Muller, R. Ramesh, N. A. A. Spaldin, and D. Meier, Functional electronic inversion layers at ferroelectric domain walls, Nat. Mater. **16,** 622 (2017).

[16] D. Meier, Functional domain walls in multiferroics, J. Phys. Condens. Matter **27,** 463003 (2015).

[17] Z. Liu, B. Yang, W. Cao, E. Fohtung, and T. Lookman, Enhanced Energy Storage with Polar Vortices in Ferroelectric Nanocomposites, Phys. Rev. Applied **8,** 034014 (2017).

[18] Y. Nahas, S. Prokhorenko, L. Louis, Z. Gui, I. Kornev, and L. Bellaiche, Discovery of stable skyrmionic state in ferroelectric nanocomposites, Nat. Commun. **6,** 8542 (2015).

[19] I. I. Naumov, L. Bellaiche, and H. Fu, Unusual phase transitions in ferroelectric nanodisks and nanorods, Nature (London) **432,** 737 (2004).

[20] A. Schilling, D. Byrne, G. Catalan, K. G. Webber, Y. A. Genenko, G. S. Wu, J. F. Scott, and J. M. Gregg, Domains in ferroelectric nanodots, Nano Lett. **9,** 3359 (2009).

[21] A. K. Yadav, C. T. Nelson, S. L. Hsu, Z. Hong, J. D. Clarkson, C. M. Schlepütz, A. R. Damodaran, P. Shafer, E. Arenholz, L. R. Dedon, D. Chen, A. Vishwanath, A. M. Minor, L. Q. Chen, J. F. Scott, L. W. Martin, R. Ramesh, C. M. Schlepüetz, A. R. Damodaran, P. Shafer, E. Arenholz, L. R. Dedon, D. Chen, A. Vishwanath, A. M. Minor, L. Q. Chen, J. F. Scott, L. W. Martin, and R. Ramesh, Observation of polar vortices in oxide superlattices, Nature (London) **530,** 198 (2016).

[22] S. Das, Y. L. Tang, Z. Hong, M. A. P. Gonçalves, M. R. McCarter, C. Klewe, K. X. Nguyen, F. Gómez-Ortiz, P. Shafer, E. Arenholz, V. A. Stoica, S. L. Hsu, B. Wang, C. Ophus, J. F. Liu, C. T. Nelson, S. Saremi, B. Prasad, A. B. Mei, D. G. Schlom, J. Íñiguez, P. García-Fernández, D. A. Muller, L. Q. Chen, J. Junquera, L. W. Martin, and R. Ramesh, Observation of room-temperature polar skyrmions, Nature (London) **568,** 368 (2019).

[23] A. R. Damodaran, J. D. Clarkson, Z. Hong, H. Liu, A. K. Yadav, C. T. Nelson, S.-L. Hsu, M. R. McCarter, K.-D. Park, V. Kravtsov, A. Farhan, Y. Dong, Z. Cai, H. Zhou, P. Aguado-Puente, P. García-Fernández, J. Íñiguez, J. Junquera, A. Scholl, M. B. Raschke, L.-Q. Chen, D. D. Fong, R. Ramesh, and L. W. Martin, Phase coexistence and electric-field control of toroidal order in oxide superlattices, Nat. Mater. **16,** 1003 (2017).

[24] P. Shafer, P. García-Fernández, P. Aguado-Puente, A. R. Damodaran, A. K. Yadav, C. T. Nelson, S.-L. Hsu, J. C. Wojdeł, J. Íñiguez, L. W. Martin, E. Arenholz, J. Junquera, and R. Ramesh, Emergent chirality in the electric polarization texture of titanate superlattices, Proc. Natl. Acad. Sci. U.S.A. **115,** 915 (2018).

[25] A. K. Yadav, K. X. Nguyen, Z. Hong, P. García-Fernández, P. Aguado-Puente, C. T. Nelson, S. Das, B. Prasad, D. Kwon, S. Cheema, A. I. Khan, C. Hu, J. Íñiguez, J. Junquera, L. Q. Chen, D. A. Muller, R. Ramesh, and S. Salahuddin, Spatially resolved steady-state negative capacitance, Nature (London) **565,** 468 (2019).

[26] J. A. Mundy, C. M. Brooks, M. E. Holtz, J. A. Moyer, H. Das, A. F. Rébola, J. T. Heron, J. D. Clarkson, S. M. Disseler, Z. Liu, A. Farhan, R. Held, R. Hovden, E. Padgett, Q. Mao, H. Paik, R. Misra, L. F. Kourkoutis, E. Arenholz, A. Scholl, J. A. Borchers, W. D. Ratcliff, R. Ramesh, C. J. Fennie, P. Schiffer, D. A. Muller, and D. G. Schlom, Atomically engineered ferroic layers yield a room-temperature magnetoelectric multiferroic, Nature (London) **537,** 523 (2016).

[27] E. Magome, C. Moriyoshi, Y. Kuroiwa, A. Masuno, and H. Inoue, Noncentrosymmetric Structure of $LuFeO_3$ in Metastable State, Jpn. J. Appl. Phys. **49,** 09ME06 (2010).

[28] H. Das, A. L. Wysocki, Y. Geng, W. Wu, and C. J. Fennie, Bulk magnetoelectricity in the hexagonal manganites and ferrites, Nat. Commun. **5,** 2998 (2014).

[29] W. Wang, J. Zhao, W. Wang, Z. Gai, N. Balke, M. Chi, H. N. Lee, W. Tian, L. Zhu, X. Cheng, D. J. Keavney, J. Yi, T. Z. Ward, P. C. Snijders, H. M. Christen, W. Wu, J. Shen, and X. Xu, Room-Temperature Multiferroic Hexagonal LuFeO$_3$ Films, Phys. Rev. Lett. **110,** 237601 (2012).

[30] S. M. Disseler, J. A. Borchers, C. M. Brooks, J. A. Mundy, J. A. Moyer, D. A. Hillsberry, E. L. Thies, D. A. Tenne, J. Heron, M. E. Holtz, J. D. Clarkson, G. M. Stiehl, P. Schiffer, D. A. Muller, D. G. Schlom, and W. D. Ratcliff, Magnetic Structure and Ordering of Multiferroic Hexagonal LuFeO$_3$, Phys. Rev. Lett. **114,** 217602 (2015).

[31] J. A. Moyer, R. Misra, J. A. Mundy, C. M. Brooks, J. T. Heron, D. A. Muller, D. G. Schlom, and P. Schiffer, Intrinsic magnetic properties of hexagonal LuFeO$_3$ and the effects of nonstoichiometry, APL Mater. **2,** 012106 (2014).

[32] D. Niermann, F. Waschkowski, J. de Groot, M. Angst, and J. Hemberger, Dielectric Properties of Charge-Ordered LuFe$_2$O$_4$ Revisited: The Apparent Influence of Contacts, Phys. Rev. Lett. **109,** 016405 (2012).

[33] S. Lafuerza, J. García, G. Subías, J. Blasco, K. Conder, and E. Pomjakushina, Intrinsic electrical properties of LuFe$_2$O$_4$, Phys. Rev. B **88,** 085130 (2013).

[34] A. D. Christianson, M. D. Lumsden, M. Angst, Z. Yamani, W. Tian, R. Jin, E. A. Payzant, S. E. Nagler, B. C. Sales, and D. Mandrus, Three-Dimensional Magnetic Correlations in Multiferroic LuFe$_2$O$_4$, Phys. Rev. Lett. **100,** 107601 (2008).

[35] S. Fan, Site-specific spectroscopic measurement of spin and charge in $(LuFeO_3)_m/(LuFe_2O_4)1$ multiferroic superlattices, Nat. Commun. **11,** 5582 (2020).

[36] L. Li, P. Gao, C. T. Nelson, J. R. Jokisaari, Y. Zhang, S. J. Kim, A. Melville, C. Adamo, D. G. Schlom, and X. Pan, Atomic Scale Structure Changes Induced by Charged Domain Walls in Ferroelectric Materials, Nano Lett. **13,** 5218 (2013).

[37] B. B. Van Aken, T. T. M. Palstra, A. Filippetti, and N. A. Spaldin, The origin of ferroelectricity in magnetoelectric YMnO$_3$, Nat. Mater. **3,** 164 (2004).

[38] C. J. Fennie and K. M. Rabe, Ferroelectric transition in YMnO$_3$ from first principles, Phys. Rev. B **72,** 1 (2005).

[39] S. Artyukhin, K. T. Delaney, N. A. Spaldin, and M. Mostovoy, Landau theory of topological defects in multiferroic hexagonal manganites, Nat. Mater. **13,** 42 (2014).

[40] M. Lilienblum, T. Lottermoser, S. Manz, S. M. Selbach, A. Cano, and M. Fiebig, Ferroelectricity in the multiferroic hexagonal manganites, Nat. Phys. **11,** 1070 (2015).

[41] S. H. Skjærvø, Q. N. Meier, M. Feygenson, N. A. Spaldin, S. J. L. Billinge, E. S. Bozin, and S. M. Selbach, Unconventional Continuous Structural Disorder at the Order-Disorder Phase Transition in the Hexagonal Manganites, Phys. Rev. X **9,** 031001 (2019).

[42] A. Cano, Hidden order in hexagonal RMnO3 multiferroics (R = Dy–Lu, In, Y, and Sc), Phys. Rev. B **89,** 214107 (2014).

[43] See Supplemental Material at http://link.aps.org/supplemental/10.1103/PhysRevLett.126.157601 for a description of the materials and methods along with 10 supplemental figures.

[44] J. Nordlander, M. Campanini, M. D. Rossell, R. Erni, Q. N. Meier, A. Cano, N. A. Spaldin, M. Fiebig, and M. Trassin, The ultrathin limit of improper ferroelectricity, Nat. Commun. **10,** 5591 (2019).

[45] X. Wang, M. Mostovoy, M. G. Han, Y. Horibe, T. Aoki, Y. Zhu, and S.-W. Cheong, Unfolding of Vortices into Topological Stripes in a Multiferroic Material, Phys. Rev. Lett. **112,** 247601 (2014).

Supplementary Information on
Dimensionality-induced change in topological order in multiferroic oxide superlattices

Megan E. Holtz[1,2], Elliot S. Padgett[1], Rachel Steinhardt[2], Charles M. Brooks[2], Dennis Meier[3], Darrell G. Schlom[2,4], David A. Muller[1,4], Julia A. Mundy[1,5]

[1] School of Applied and Engineering Physics, Cornell University, Ithaca, New York 14853, USA

[2] Department of Materials Science and Engineering, Cornell University, Ithaca, New York 14853, USA

[3] Department of Materials Science and Engineering, Norwegian University of Science and Technology, 7491 Trondheim, Norway

[4] Kavli Institute at Cornell for Nanoscale Science, Ithaca, New York 14853, USA

[5] Department of Physics, Harvard University, Cambridge, Massachusetts 02138 USA

Materials and Methods

Thin films of $(LuFeO_3)_m/(LuFe_2O_4)$ were grown by reactive-oxide molecular-beam epitaxy in a Veeco GEN10 system on (111) $(ZrO_2)_{0.905}(Y_2O_3)_{0.095}$ (or 9.5 mol% yttria-stabilized zirconia) (YSZ) substrates, as described in Ref [24]. Thin films of $(LuFeO_3)/(InFeO_3)$ superlattices were also grown by reactive-oxide molecular-beam epitaxy in a Veeco GEN10 system on (111) YSZ at 900°C in 1e-6 Torr 10% ozone/ oxygen environment. $LuFeO_3$ was calibrated as in the previous work – except here the Lu and Fe sources were flux-matched and the $LuFeO_3$ layers were grown by codeposition. The In source was calibrated by a quartz crystal monitor, and the $InFeO_3$ was grown by shuttered growth. X-ray diffraction (XRD) reciprocal space maps (RSM) were taken using Cu-Kα1 around the YSZ substrate 422 reflection on a Panalytical Empyrean X-ray diffractometer. For $LuFeO_3$ grown on YSZ, the strain relaxes within the first unit cell of growth, as evidenced by XRD RSM and STEM images (SI Fig. 7) and in-situ RHEED during growth.

The magnetic properties have been previously described for $LuFeO_3$ [30], $LuFe_2O_4$ [33], and the superlattices [25]. In summary, $LuFeO_3$ is a canted antiferromagnet below 147 K and thus has no net magnetic moment at room temperature. The $LuFe_2O_4$, on the other hand, has a ferrimagnetic moment below 240 K. In the superlattices, the magnetization vs. temperature curves have similar transitions compared to $LuFe_2O_4$, indicating that the magnetic characteristics of the superlattices originate from the $LuFe_2O_4$ – which has been further corroborated by beamline spectroscopy. In the superlattices, the magnetic transition temperature is raised to room-temperature by the lutetium distortions imposed by the ferroelectric $LuFeO_3$, breaking the magnetic frustration.

Cross-sectional TEM specimens were prepared using an FEI Strata 400 Focused Ion Beam (FIB) with a final milling step of 2 keV to reduce surface damage. High-resolution HAADF-STEM images were acquired on a 100-keV Nion UltraSTEM, a fifth-order aberration-corrected microscope with a 25 mrad convergence angle, and a 300-keV FEI Titan Themis with

a 21.4 mrad convergence angle. EELS was acquired on the NION with a beam current of 100 pA and collection angle of 60 mrad.

The lutetium distortions were quantified from HAADF-STEM images. Several images were acquired with fast dwell time (<1-6 us) and averaged to reduce scan noise. Lutetium atomic positions were determined through segmentation using a threshold plus watershed algorithm, followed by two-dimensional Gaussian fitting procedure that was implemented in MATLAB.

The position of each atom was then compared to its neighboring atom on each side in the same atomic plane, and the order parameters fit using equation in Fig. 1a in Ref. 12. To garner statistics for each layering, the order parameters, atomic positions, and layer type m were collected for over 14,000 nm^2 (data from 142,640 atomic columns) of material. We did not include regions in the analysis where antiphase boundaries and step edges in the film are present, so that these obvious defects in the crystallinity do not impact statistics across different layers. We also excluded the first $LuFeO_3$ block grown directly on the substrate, since clamping from the substrate/film interface suppresses ferroelectricity (which is not observed at the $LuFeO_3$ / $LuFeO_4$ interface). This analysis was performed in MATLAB using homemade functions and those in the image processing toolbox.

To collect statistics of the presence of domain walls and their angles (Fig 1 d-e, SI Fig 5), the domain walls were found first by segmenting the domains (by rounding the continuous order parameter, Φ) and finding the intersections where the domain walls lie. Then, moving atom-by-atom along in the horizontal, in-plane direction of the film for each double iron layer and across each $LuFeO_3$ block, statistics of the occurrence of domain walls were tallied for each m: if there was a domain wall present, what the relative change in phase $\Delta\Phi$ was, and if it was within the $LuFeO_3$ block, what the local angle of the wall was.
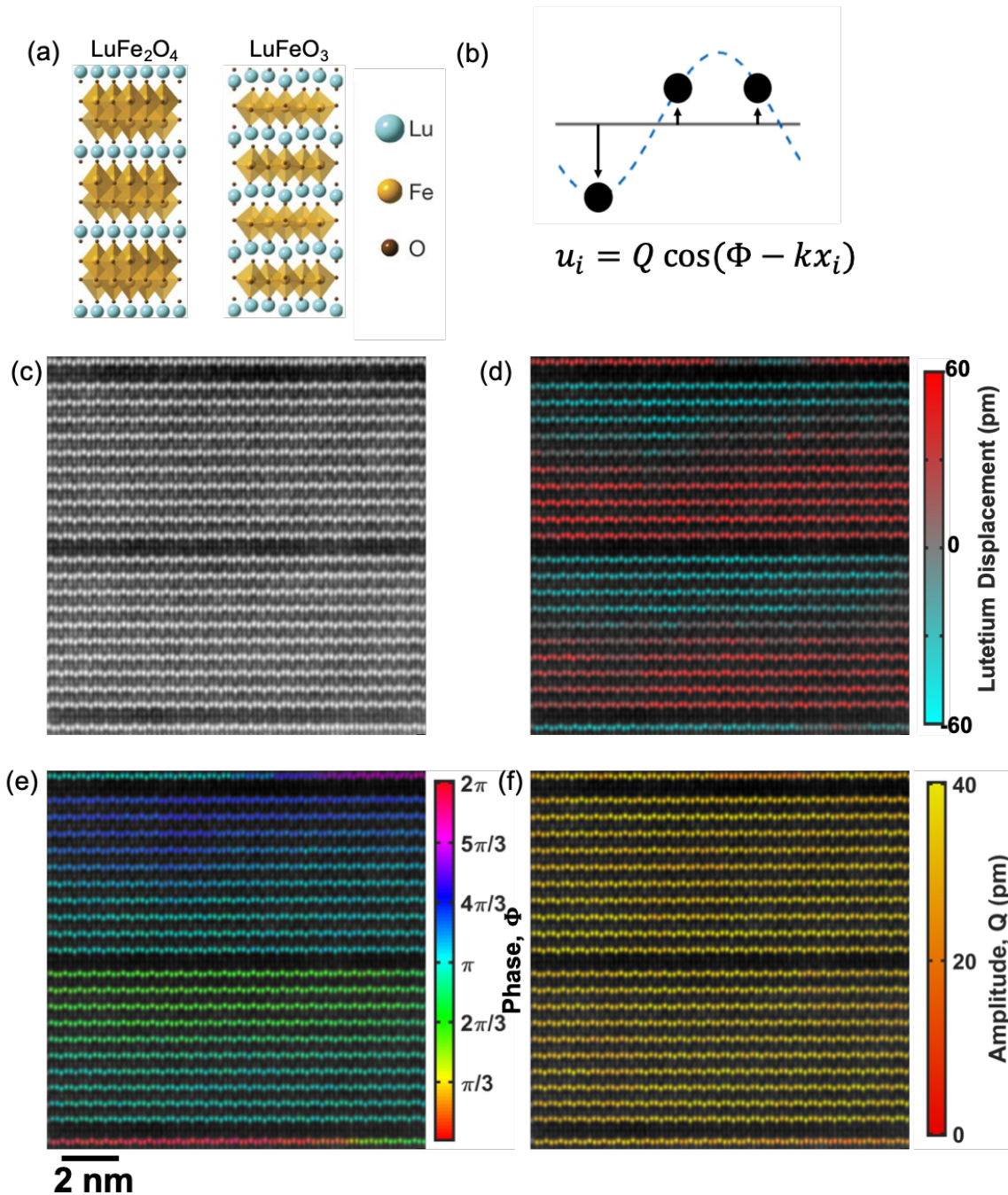
SI Figure 1. Mapping lutetium displacements in STEM allows measurement of the local polarization and order parameter in the film. a: Cartoon of the crystal structures of the two end members. b: Cartoon of Lu displacements, relating the displacement of the Lu atoms from their mean position (u) to the components of the order parameter, Φ and Q with position x across the film, where k is $2\pi/3x_o$, where x_o is the in plane atomic spacing. c: STEM image of the $(LuFeO_3)_9/(LuFe_2O_4)$ superlattice. d: color overlay of the image representing the polarization – directly interpretable from the lutetium displacements. e: Φ overlay showing different trimerization domains and f: Q overlay, showing that the amplitude of trimerization is relatively uniform in the superlattice.
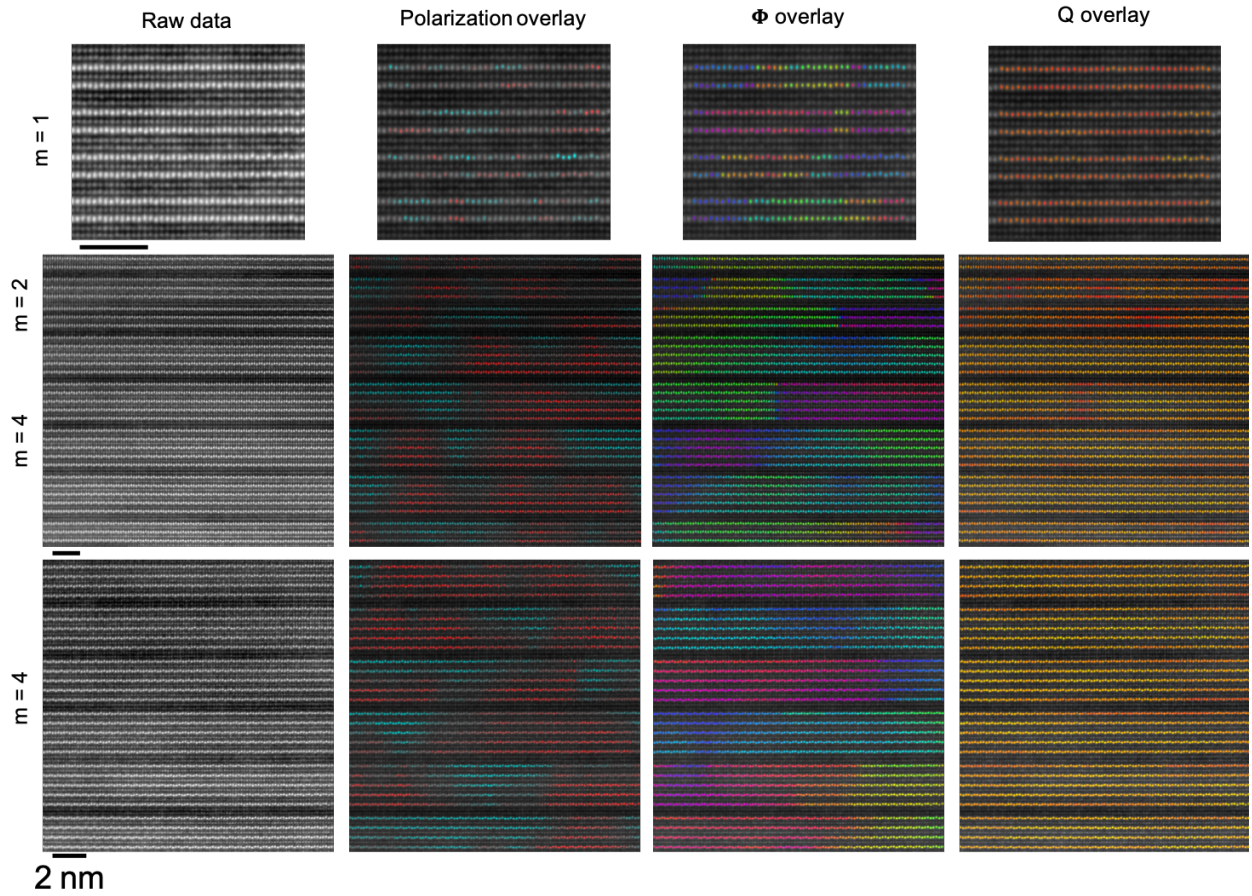
SI Fig. 2. Large field of view images for m = 1, 2 and 4 $(LuFeO_3)_m$ / $LuFe_2O_4$. Raw images as well as polarization, Φ and Q color overlays are shown, using the same color scale as SI Fig 1.
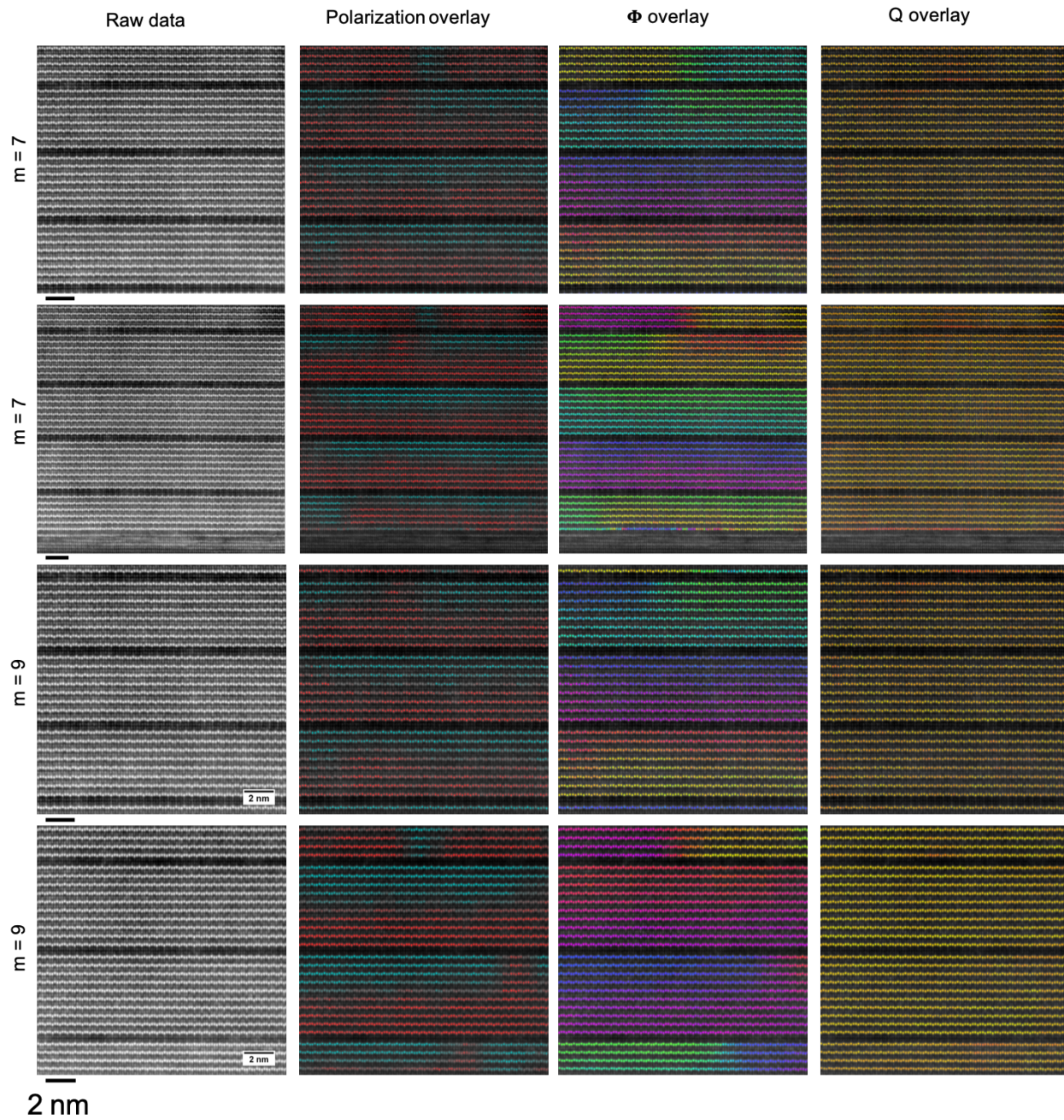
SI Fig. 3. Large field of view images for $m = 7$ and 9 $(LuFeO_3)_m$ / $LuFe_2O_4$. Raw images as well as polarization, Φ and Q color overlays are shown, using the same color scale as SI Fig 1.
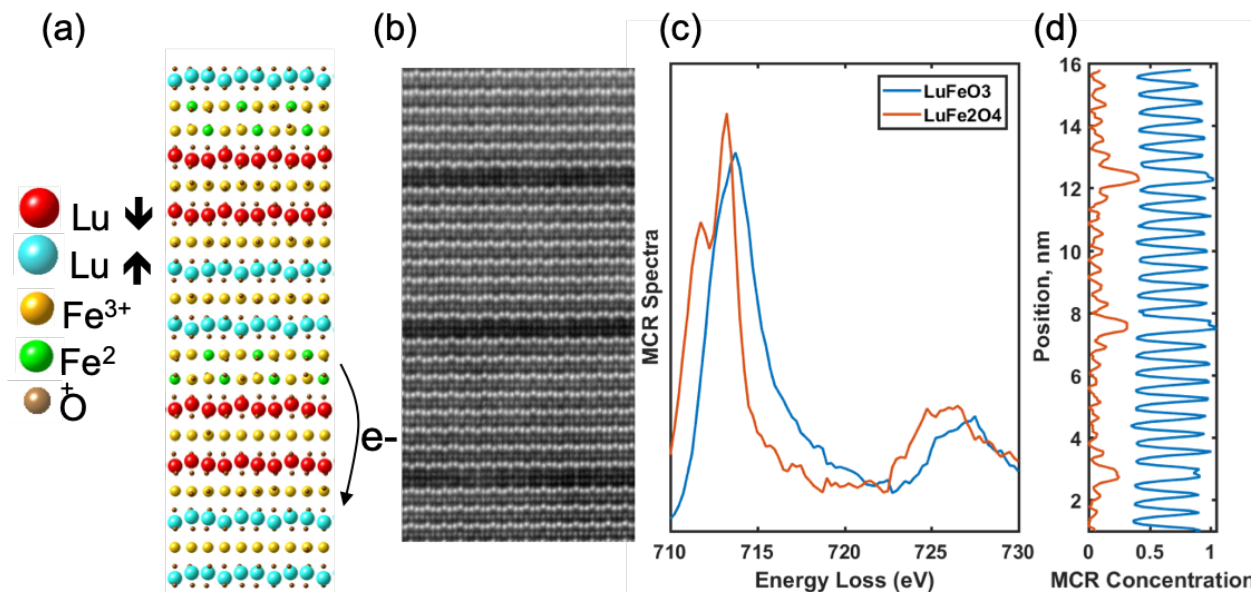
SI Fig. 4. Charge compensation of domain walls in the $(LuFeO_3)_m/(LuFe_2O_4)$ superlattice. (a) DFT showing the regular domain structure predicting more Fe^{3+} on the double iron layer for a m = 3 superlattice. (b) ADF image showing region where EELS spectra were acquired. (c) MCR extracted spectra and (d) concentrations, showing a slight reduction in iron valence on the "$LuFe_2O_4$"-like spectra in the m = 7 superlattice.
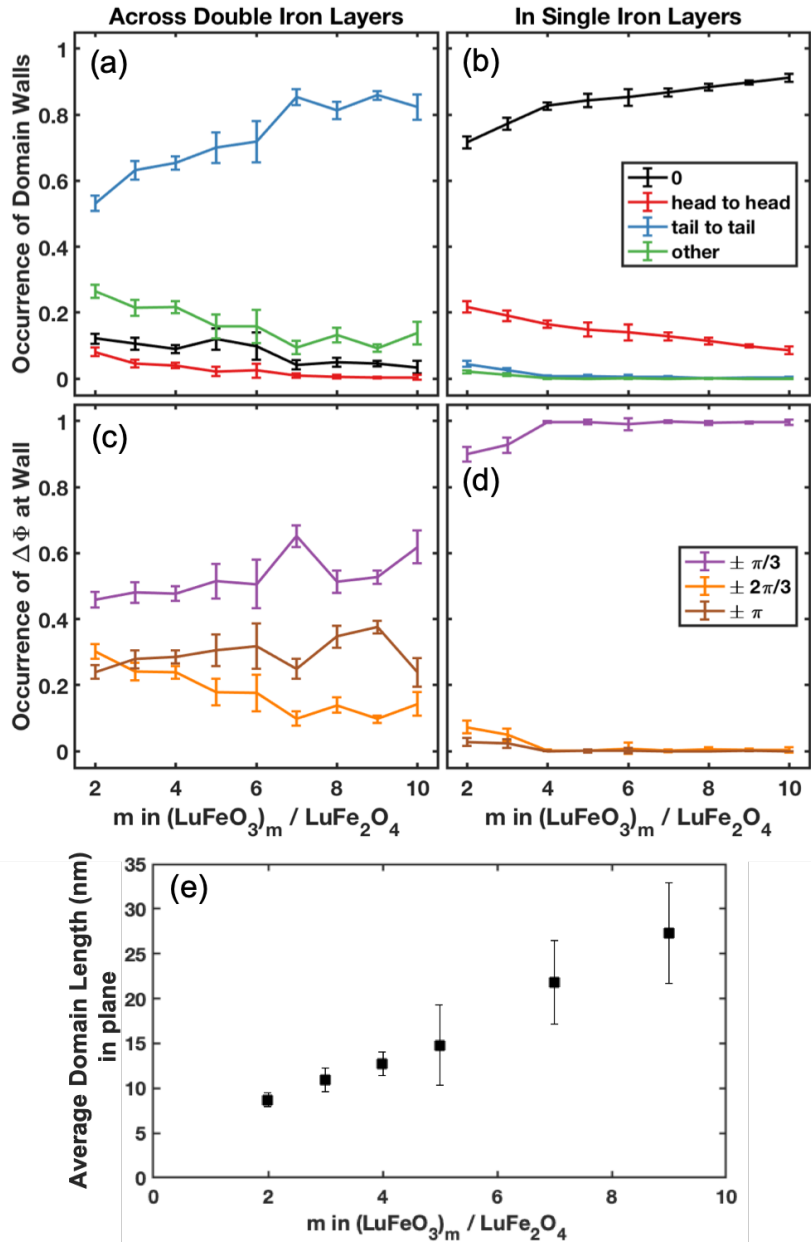
SI Fig. 5. Occurrences of different types of domain walls going across the double iron layers and within the $LuFeO_3$ blocks. The occurrences are normalized per in-plane length, as measured unit-cell by unit-cell. (a) and (b) are occurrences of domain walls in the out of plane direction, normalized per atom measured. Head-to-head domain walls rarely occur across $LuFe_2O_4$ layers, instead occurring in the $LuFeO_3$ blocks. Tail-to-tail walls are dominant across $LuFe_2O_4$ layers, especially with higher m. (c) and (d) are distributions of the phase change across a domain wall, normalized per atom on a domain wall. In (c), across the double iron layer, we note that a phase change of $\Delta\Phi = \pm 2\pi/3$ cannot correspond to a tail to tail configuration, since the polarization direction is the same. These occurrences are coming from the double iron layers near the half-vortex cores, and drop off for higher m, corresponding to the stabilization of the tail to tail polarization configuration. Comparing the prevalence of $\Delta\Phi = \pm\pi/3$ to $\Delta\Phi = \pm\pi$, it appears that $\pm\pi/3$ is twice as likely as $\pm\pi$, however, there are two measurable states for the former and only

one for the latter (ie. $\Delta\Phi = +\pi$ and $-\pi$ are equivalent). So if the domains on opposite sides of the double iron layer are randomly populated, we would expect to observe twice as many $\Delta\Phi = \pm\pi/3$ as $\Delta\Phi = \pm\pi$, which appears to be the case. Within the $LuFeO_3$ block (d), a large majority of domain changes are $\pm\pi/3$, with essentially all of the walls for $m > 3$. For $m = 2, 3$, less than 10% of the walls deviate from $\Delta\Phi = \pm\pi/3$ – which is possibly stabilized by defects and by the flatter energy landscape (as observed in Fig. 4). (e) The statistical length of the charged domain walls in-plane in the $LuFeO_3$ block. This was measured by counting across the images how often the end of the charged domain wall was observed (at a fractional vortex) per length, and then inverting it, to minimize field of view artifacts. We observe a linear increase in the in-plane charged domain wall length as a function of m.
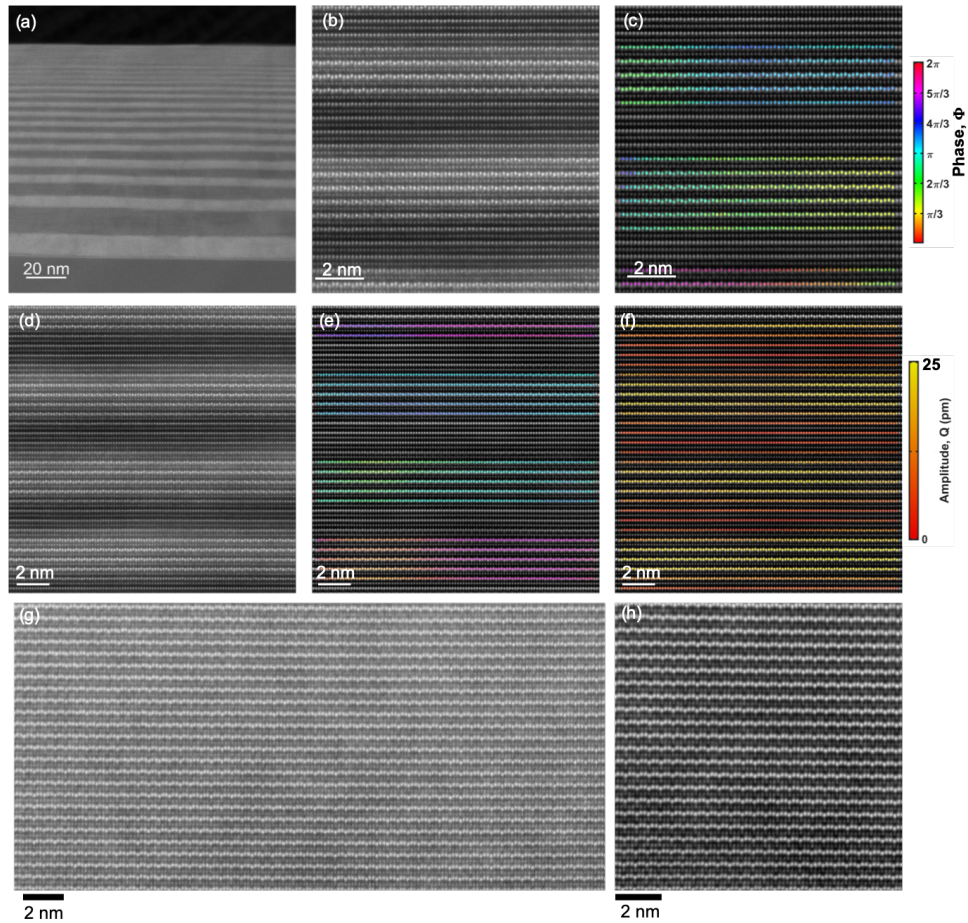

SI Fig. 6. $LuFeO_3$ ferroelectric layers grown in between $InFeO_3$ paraelectric layers. (a) HAADF image overview of superlattice sample grown for TEM, where bright layers are $LuFeO_3$ and dark layers are $InFeO_3$. (b-c) raw image and phase overlay in $LuFeO_3$ layers of 4-5 layers thick, showing no clear domain architecture or pinned domain walls. (d-f) raw image, phase overlay, and trimerization amplitude overlay showing no clear domain structure and that the amplitude is damped near the $InFeO_3$ layers. (g-h) Images of a 200 nm thick $LuFeO_3$ single phase film on YSZ. The sample is monodomain.
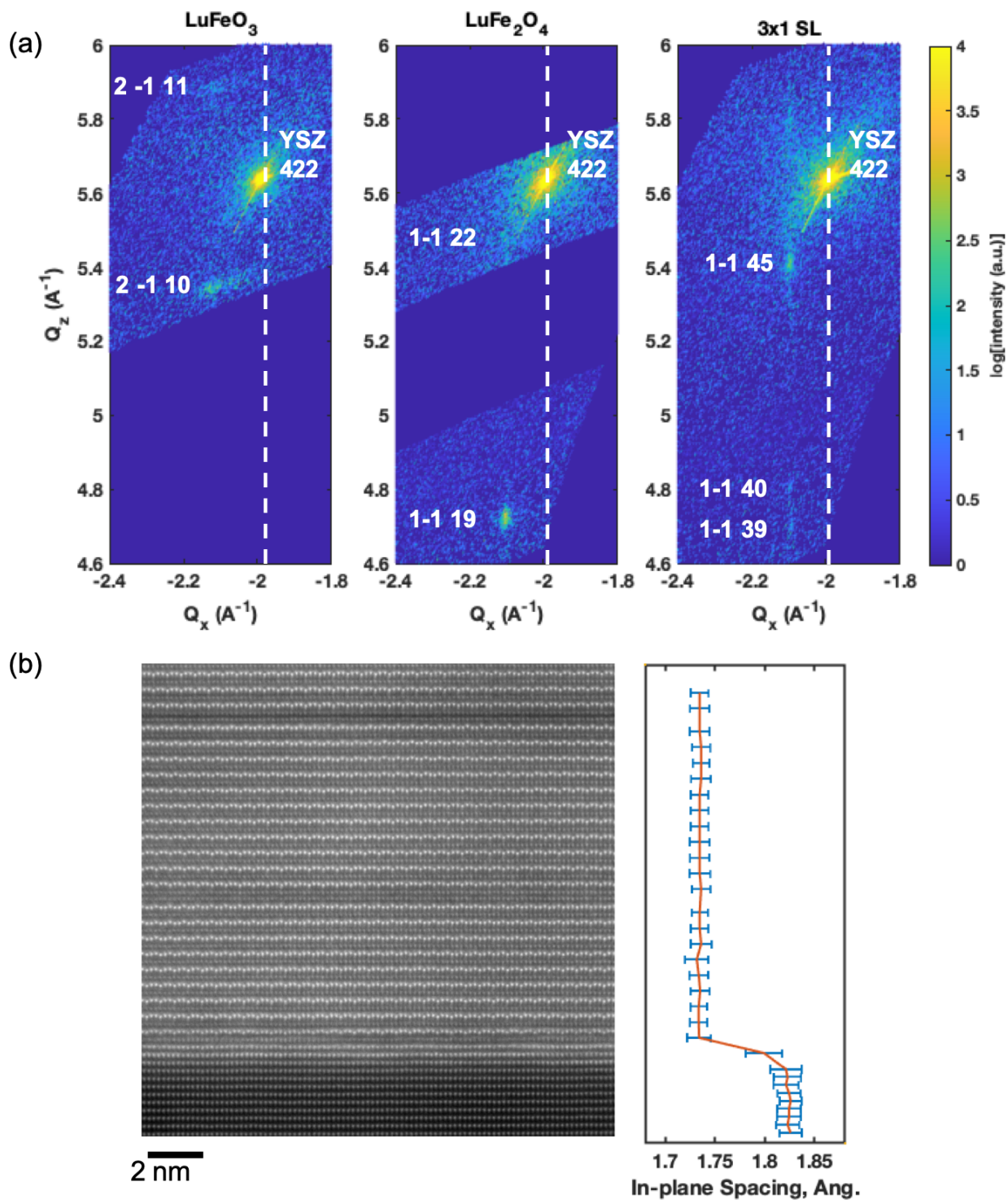
SI Fig. 7. The in-plane lattice spacing of a LuFeO$_3$, LuFe$_2$O$_4$, and $m = 3$ (LuFeO$_3$)$_3$/(LuFe$_2$O$_4$) superlattice measured by reciprocal space mapping (a). Q_x represents the in-plane lattice spacing, showing a clear difference between the YSZ substrate peak and the film peaks. (b) STEM measurements of the in-plane lattice parameter, which relaxes within the first unit cell in the film.
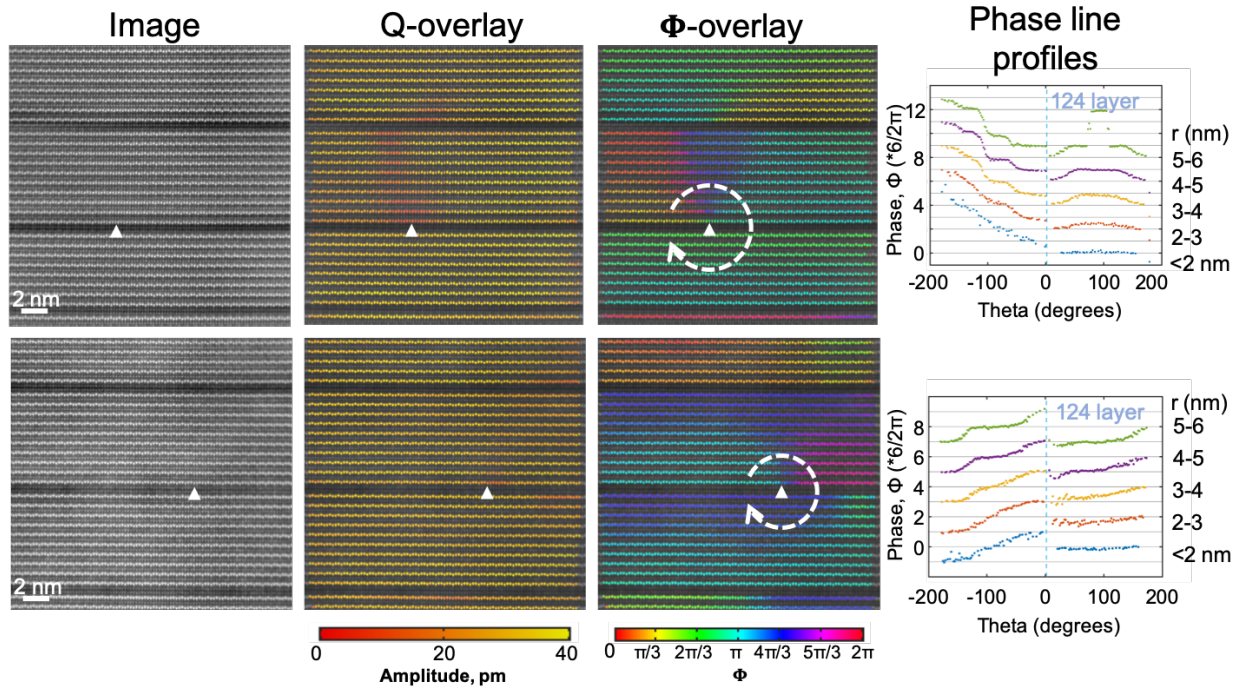
SI Fig. 8. Comparison of the order parameter changing around a full vortex (top row) and a partial vortex (bottom row) for $m = 9$ $(LuFeO_3)_m/(LuFe_2O_4)$ superlattices – showing the raw image, the amplitude color overlay, and the phase color overlay with the center of the vortex marked. The amplitude Q drops near the full vortex where the domain walls are close together, and only slightly perceptibly drops at the 3-fold vortex near the center where the walls come together. The phase image highlights the 6 domains coming together on the top and 3 domains coming together on the bottom. On the right, the phase Φ is plotted as a function of the angle around the center for circles of different radii. For both the full vortex and partial vortex, near the core the phase starts to wind continuously while winding in a step-wise fashion further from the core.
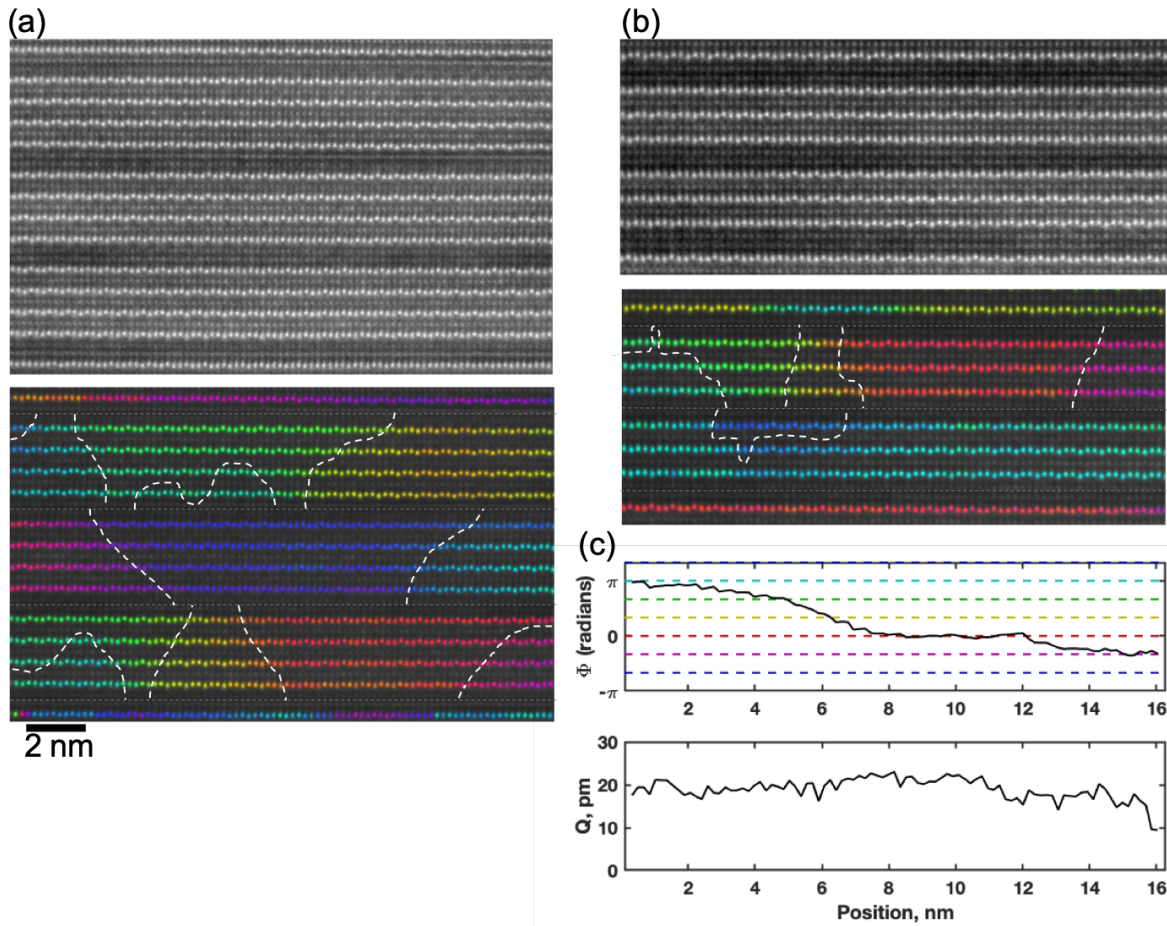
SI Fig 9. Raw images and phase overlays showing phase winding near the neutral walls in the lower m ($m = 3$ in a, 2 in b) $(LuFeO_3)_m/(LuFe_2O_4)$ superlattices. In (c) are line plots of the order parameter Φ and Q for the top layer in (b), showing that when the vertical domains are close together, the phase winds linearly while Q remains constant.
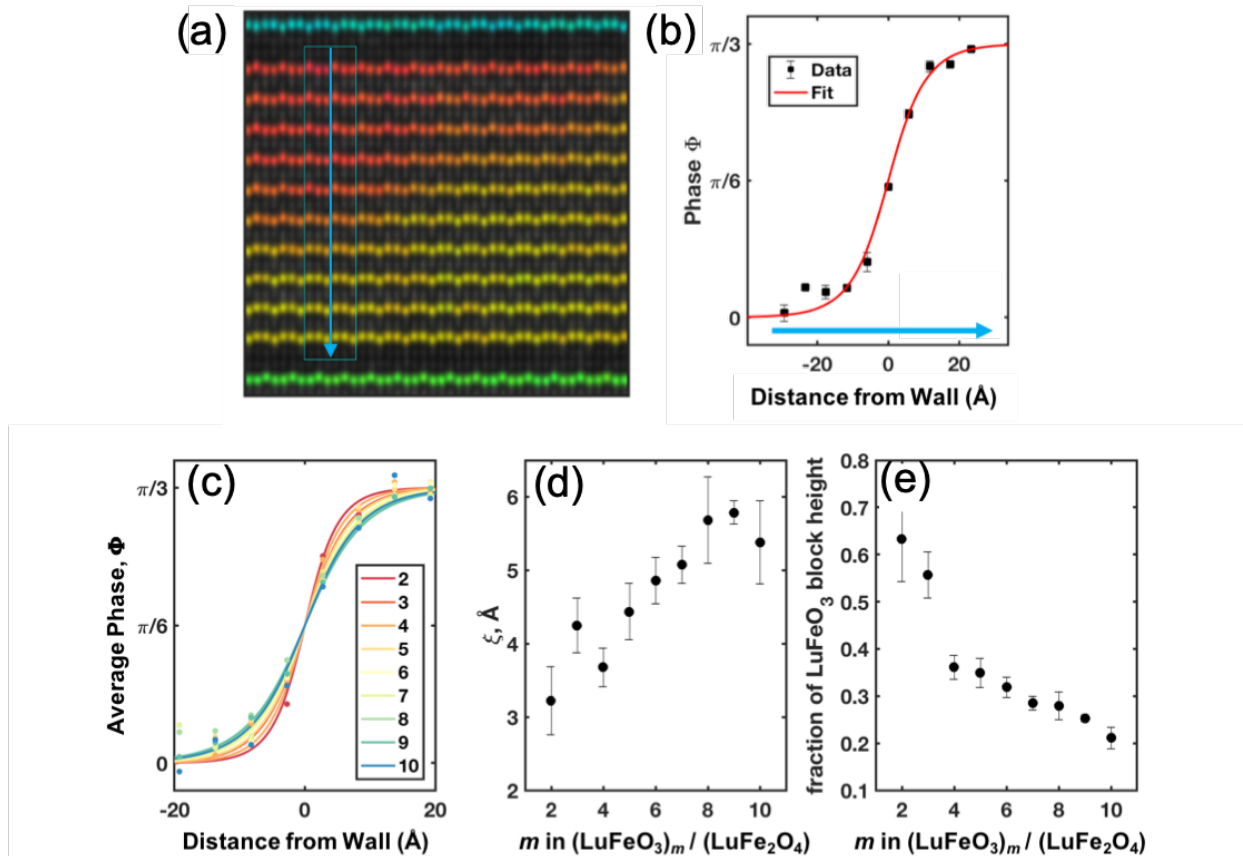
SI Fig 10. The order parameter Φ going across a charge domain wall in the LuFeO$_3$ blocks as a function of LuFeO$_3$ thickness, m. a: STEM image of an $m = 9$ superlattice, with cyan box and arrow indicating where the phase Φ is plotted in (b). (b) How the phase evolves across the domain wall. (c) how the phase evolves as a function of distance from the center of the domain for the charged domain walls for different m. (d) the width of the domain walls ξ_6 from Landau theory, where the domain walls are thinner in the smaller layers and thicker in the wider layers – suggesting electrostatic confinement affects domain width. (c) the 20-80% width of the domain as a fraction of the LuFeO$_3$ block height. For smaller layers, the domain wall takes up more than half of the volume of the LuFeO$_3$ block.